ROYAL SOCIETY
OF CHEMISTRY

PAPER

Check for updates

Polyoxometalate-pillared metal–organic frameworks synthesized by surfactant-assisted strategy and incorporated with carbon nanotubes for energy storage†

Xi-Ya Yang, [ID] [ac] Wen-Jing Li,[a] Zeng-Long Tan,[a] Jing-Quan Sha, [ID] *[a] Zhi-Bo Tong,[a] Yu Zhang [ID] *[b] and Ya-Qian Lan [ID] *[b]

The application of surfactant or surfactant-assisted media to grow polyoxometalate (POM)-based MOFs (POMOFs) is extremely scarce. In this work, for the first time, we use water-polyethylene glycol (PEG) 400 mixed media to synthesize two new crystalline POM-pillared three-dimensional porous arrays, $[Co_7(Trz)_{12}(H_2O)_8][HPX_{12}O_{40}(VO)_2]\cdot12H_2O$ (X = Mo for **Co-PMo** and X = W for **Co-PW**, Trz = 1,2,4-triazole). By employing a simple sonication-driven functionalization strategy, **Co-PMo**/CNTs (PCNT-*n*) nanocomposites with increased effective sites, enhanced specific surface area and excellent conductivity are fabricated. The resulting PCNT-2 nanocomposite shows an excellent reversible capacity of 820 mA h g^{-1} after 100 cycles and outstanding rate capability as an anode for lithium batteries. After the initial decay, the PCNT-2 electrode can bear a current density of 2000 mA g^{-1} over 450 cycles without obvious capacity loss. Meanwhile, the mechanism of lithium storage in PCNT-2 is discussed using X-ray photoelectron spectroscopy (XPS). Moreover, the PCNT-2 nanocomposite exhibits the hybrid behavior of battery and supercapacitor according to the electrochemical kinetic analyses. This might open new avenues for the design of crystalline POM-based materials or their nanocomposites to achieve high-performance energy storage.

Introduction

Polyoxometalates (POMs), as early polynuclear transition-metal oxide clusters, have been widely explored in the field of material chemistry, owing to their versatile structure, high thermal stability and inherent redox properties.[1–3] To maximize the advantages of POMs, the design and synthesis of POM-based metal–organic frameworks (POMOFs) have been developed as an efficient strategy that can realize an excellent dispersal of POMs at the molecular level to expose more accessible sites and can combine the advantages of both to produce new functions.[4–7] In particular, the appropriate porosity or channels in POMOFs facilitate the accessibility of substrates or reactants to active POM species, enhancing the performance of POMOF

applications. At present, hydrothermal/solvothermal methods are the conventional ways to synthesize POMOF materials. However, the disadvantages of common solvents, such as low boiling point[8] and limited solubility for organic and inorganic components, have hampered the further exploration of novel structures. Thus, new synthesis strategies are required for preparing crystalline POMOFs with novel structures and interesting properties.

Surfactants with thermal stability and industrial abundance have been widely applied in controlling the sizes and shapes of nanocrystals and the pore sizes and phases of porous materials;[9–14] thus, using surfactants as reaction media to synthesize novel crystalline materials is highly expected. In recent years, many research groups have employed surfactant media to prepare crystal chalcogenides and MOFs. For example, Zhang and colleagues reported several crystalline chalcogenides[15,16] and MOFs[8,17–21] that have been synthesized by a surfactant-thermal method. However, the synthesis of novel POMOFs by a surfactant/surfactant-assisted thermal method still remains extremely rare, and is limited as the sole example of a $[VW_{12}O_{40}]^{4-}$ based Zn/triazole framework synthesized by a polyethylene glycol (PEG) 1500-assisted method reported by our group.[22]

[a]Department of Chemistry and Chemical Engineering, Jining University, Shandong 273155, China. E-mail: shajq2002@126.com

[b]School of Chemistry and Materials Science, Nanjing Normal University, Nanjing 210023, P. R. China. E-mail: yqlan@njnu.edu.cn; yuzhang803@163.com

[c]Department of Chemistry, University of Science and Technology Beijing, Beijing 100083, China

† Electronic supplementary information (ESI) available: Experimental methods and supporting figures and tables. CCDC 1877166 and 1935987. For ESI and crystallographic data in CIF or other electronic format see DOI: 10.1039/d0ta08976a

25316 | *J. Mater. Chem. A*, 2020, 8, 25316–25322

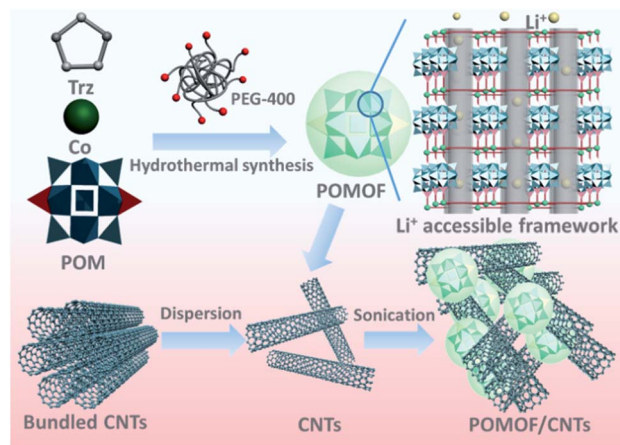This journal is © The Royal Society of Chemistry 2020

When it comes to the applications of POM-based hybrids, recently, POMs show potential as electrode materials for lithium ion batteries (LIBs), especially molybdenum-based POMs.[23–25] For example, Awaga and co-workers found that $[PMo_{12}O_{40}]^{3-}$ could undergo a reversible 24 electrons redox during charging/discharging between $[PMo_{12}O_{40}]^{3-}$ and $[PMo_{12}O_{40}]^{27-}$, while maintaining its structural integrity.[26,27] In recent years, our group has intensively fabricated a series of novel POMOFs-based electrodes for LIBs, which show excellent performance with high capacities.[28–32] Despite these exciting fundamental studies, practical applications of POMOFs in the most cutting-edge LIBs still lag behind due to their poor capability arising from the poor electrical conductivity. To address this issue, the combination of POMOFs with conductive carbon matrices (*e.g.* reduced graphene oxide (RGO),[33,34] carbon nanotubes (CNTs),[35,36] and Ketjen black carbon (KB)[37]) has been shown to be an effective strategy. Among these carbon matrices, carbon nanotubes (CNTs) are actively being developed because of their excellent electron conductivity and highly delocalized p-conjugated electron system. As far as we know, no research has been reported to integrate molybdenum-based POMs and MOFs for LIBs.

Herein, two isostructural POMOFs, $[Co_7(Trz)_{12}(H_2O)_8]$ $[HPX_{12}O_{40}(VO)_2] \cdot 12H_2O$ (X = Mo for **Co-PMo** and X = W for **Co-PW**), showing intriguing 3D POM-sandwiched frameworks, are fabricated by utilizing a PEG-400 assisted hydrothermal method for the first time. Our primary investigation indicates that the $[PMo_{12}O_{40}]$-based cobalt-triazole framework (**Co-PMo**) results in excellent LIB performances. Then, the **Co-PMo**/SWCNTs nanocomposites (PCNT-*n*) were prepared by employing a simple sonication-driven periodic functionalization strategy. Moreover, when used as anodes for LIBs, the PCNT-2 shows a reversible capacity in excess of 820 mA h g^{-1} for 100 cycles at 100 mA g^{-1} and can bear a current density of 2000 mA g^{-1} for 450 cycles without obvious capacity loss after the initial decay, which clearly boosts the LIB performance of (Scheme 1)**Co-PMo**.

Results and discussion

Black cuboid crystals of **Co-PMo** and **Co-PW** (Fig. S1, ESI†) were obtained from the reaction of the Keggin-type $[H_3PMo_{12}O_{40}]$ or $[H_3PW_{12}O_{40}]$, $Co(NO_3)_2$, Trz ligand, NH_4VO_3 and polyethyleneglycol (PEG) 400 in water at 170 °C for 3 days. Parallel test results show that the use of surfactant PEG 400 is necessary to synthesize them, or no crystals were obtained (Table S1, ESI†). We speculate that the non-ionic surfactant PEG 400 has both hydrophilic and hydrophobic groups, which not only enhance the solubility of inorganic salts and organic molecules but also efficiently direct crystal growth through strong interaction between the crystal faces and surfactants. On the other hand, when the molecular weight of PEG increases and is accompanied by chain growth, the viscosity and density of the total solution may increase, which is not suitable for crystal growth.

Single crystal X-ray diffraction analyses reveal that **Co-PMo** and **Co-PW** are isomorphous POM-based MOFs (Table S2†) of which the unit cell dimensions, volumes, related bond distances and angles are only slightly changed. Thus, we discuss

Scheme 1 Schematic illustration of the preparation of PCNT nanocomposites.

the structure of **Co-PMo** in detail as a typical example. **Co-PMo** crystallizes in tetragonal space group $C2/m$ (no. 12) and consists of two independent one-sixth of $[PMO_{12}O_{40}(VO)_2]^{3-}$ (abbreviated to PMoV) polyanion, three Co^{2+} cations, three deprotonated Trz ligand, and eight water molecules (Fig. S2, ESI†). There exist three crystallographic independent Co centers (Co1–Co3, all adopt six coordinated modes) and two POMV polyanions (PMoV-1 and PMoV-2, all adopt liner coordinated modes) and their coordination patterns are presented in Fig. S2b and c (ESI†). The Co–N and Co–O bond distances range from 2.088–2.204 Å and 2.028–2.157 Å, which is comparable to the other Co–N/O bond lengths in the structure, respectively.

The structure of **Co-PMo** can be described as a 3D POM-supported framework composed of 2D layers of $[Co_7(Trz)_{12}]_n^{2-n+}$, which are interconnected by PMoV polyanions. The 2D layers can be understood from Fig. 1a and S3.† Three Co cations are first linked by six triazole ligands in a pyrazole-like bridging mode to give a neutral trinucleate $[Co_3(Trz)_6] \cdot (\{Co_3\})$ unit. Subsequently, four such units are fused together by terminal N atoms and Co cations to form the distorted metal–organic crown $[\{Co_3(Trz)_6\}_4] \cdot (\{Co_{12}\})$. Then the $\{Co_{12}\}$ crown embraces four pendant Trz ligands that could capture a cationic Co3 center resulting in the $\{Co_{13}\}$ unit. Note that the $\{Co_{13}\}$ unit contains sixteen water molecules and the position of them are presented in Fig. S4 (ESI†), which are omitted for clarity in the following description. Finally, the $\{Co_{13}\}$ units connect each other using $\{Co_3\}$ subunits as their common vertices forming cobalt-Trz layers. The POMV polyanion is based on the well-known Keggin structure that contains twelve octahedral MoO_6 with one PO_4 tetrahedron at the center and two additional coordinated terminal $\{VO\}$ units. The two PMoV polyanions link with the Co3 center alternately forming the 1D inorganic chain (Fig. 1b). Interestingly, the two adjacent POMV cluster (POMV-1 and POMV-2) with different directions can transform each other by rotating 90 degrees along the [1 0 1] facet (Fig. S5, ESI†). As a whole, the POMV-Co chains and 2D cobalt-Trz networks fuse together fabricating a POM-supported framework with graphite-like structure, in which POMV clusters are pillared between the centers of layers (Fig. 1c, d and S6a, ESI†). From the topological
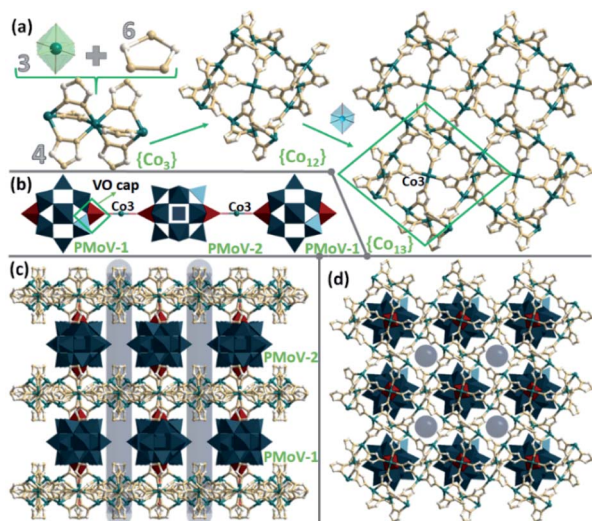
This journal is © The Royal Society of Chemistry 2020

J. Mater. Chem. A, 2020, **8**, 25316–25322 | **25317**

Fig. 1 Summary of the structure of **Co-PMo**. (a) The formation process of 2D cobalt-triazole network, (b) the 1D inorganic chain constructed by PMoV polyanions and Co3 cations, and the whole POM-supported framework along (c) [1 1 0] and (d) [0 0 1] direction.
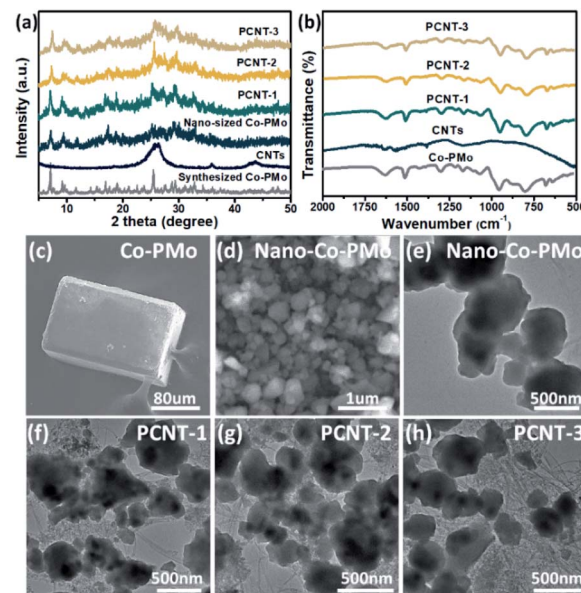

Fig. 2 (a) PXRD patterns of **Co-PMo**, CNTs, nano-sized **Co-PMo** and PCNT-n. (b) FT-IR spectra of **Co-PMo**, CNTs and PCNT-n. SEM images of (c) **Co-PMo** and (d) nano-sized **Co-PMo**. TEM images of (e) nano-sized **Co-PMo**, (f) PCNT-1, (g) PCNT-2 and (h) PCNT-3.

view, **Co-PMo** exhibits a unique (2,2,6,6,6)-connected 3D framework with an unprecedented $\{3^4 \cdot 4^2 \cdot 8^8 \cdot 12\}$ $\{3^4 \cdot 4^4 \cdot 5^4 \cdot 6^3\}^2\{8\}$ topology. In this simplification, the 2-connected nodes are POMV-1 and POMV-2, and the 6-connected nodes are the Co3 cation and two {Co3} units (Fig. S6b, ESI†).

The **Co-PMo** has been taken as an example for acting as an electrode material of Li-ion batteries. To achieve more effective sites for the battery reaction, the **Co-PMo** was nanosized via a microwave method. Single-wall carbon nanotubes (SWCNTs) were introduced to obtain the PCNT-n nanocomposites with enhanced conductivity. The structures of as-prepared **Co-PMo**, nano-**Co-PMo**, PCNT-1, PCNT-2, and PCNT-3 were characterized by powder X-ray diffraction patterns (PXRD). As shown in Fig. 2a and S7 (ESI†), all of the as-prepared samples are in good agreement with the corresponding simulated patterns, confirming the phase purity and good crystallinity. The related FT-IR spectra are shown in Fig. 2b and S8 (ESI†). Characteristic bands at 1057, 948, 870 and 791 cm^{-1} for **Co-PMo** are attributed to ν(P–O), ν(Mo=O$_d$), and ν(Mo–O$_{b/c}$–Mo) vibrations, respectively. Peaks at 1075, 956, 887 and 798 cm^{-1} for **Co-PW** are attributed to ν(P–O), ν(W=O$_d$), and ν(W–O$_{b/c}$–W) vibrations, respectively. Compared to **Co-PMo**, the peaks of PCNT-1, PCNT-2 and PCNT-3 show slight movements, indicating the effective hydrogen bonding and π–π interactions between **Co-PMo** and CNTs. Raman spectra of **Co-PMo** present an intense band at 940 cm^{-1}, and the characteristic bands of PCNT-n (λ_{ex} = 633 nm) are observed at 1350 (D band), 1576 (G band) and 2693 cm^{-1} (D* band) but also include the characteristic band of **Co-PMo**, indicating the successful fabrication of PCNT-n composite materials (Fig. S9†). The nitrogen (N2) adsorption–desorption isotherms were also used to evaluate the porous structures of **Co-PMo** and PCNT composites, and the specific surface areas are 9.32 m^2 g^{-1} for **Co-PMo**, 127.54 m^2 g^{-1} for CNTs and 45.78 m^2 g^{-1} for PCNT-2. Both **Co-PMo** and PCNT-2

have a type I isotherm, but PCNT-2 has the hysteresis loops at a relatively high-pressure range compared with **Co-PMo**, indicating that the mesoporous structures result from the stacking of **Co-PMo** and CNTs (Fig. S10 and S11†). The results show that compared with **Co-PMo**, the composite not only increases its conductivity, but also increases its surface area, which makes it easier to invade the electrolyte and obtain good battery performance.

Scanning electron microscopy (SEM) and energy dispersive spectroscopy (EDS) were employed to study the morphology and element distribution of **Co-PMo**, **Co-PW**, nano-**Co-PMo**, CNTs, PCNT-1, PCNT-2 and PCNT-3. **Co-PMo** exhibits a cuboid shape with an average size of ∼140 μm, while **Co-PMo** has a cube shape with an average size of ∼200 μm (Fig. S12, ESI†). The energy dispersive spectroscopy (EDS) shows the presence of Mo, Co, V, O, N, C and P elements for **Co-PMo**, and Mo, Co, V, O, N, C and P elements for **Co-PW**. Meanwhile, the mapping images clearly indicate the homogenous distribution of these elements. As shown in Fig. 2c–e, after grinding and the microwave reaction, the size of **Co-PMo** reduces sharply to 300–400 nm. In addition, it can be seen that the SWCNT bundles loosened upon treatment with nano-**Co-PMo**, indicating the improved dispersion of SWCNTs in the nanocomposite. Meanwhile, the intrinsic structure of nano-**Co-PMo** is retained well (Fig. 2a and b). Transmission electron microscopy (TEM) images of nano-**Co-PMo**, PCNT-1 to 3, and CNTs, are provided (Fig. 2e–h, S13 and S14†), which indicate that SWCNTs are located around nano-**Co-PMo**, and the content of SWCNTs increases with the increasing mass ratios of CNTs: from 10% to 30%. The uniformity of PCNT-2 is also verified by the elemental mapping, and the uniform distribution of Mo, C, Co, N, V, O and P are consistent with EDS spectrometry (Fig. S15, ESI†). The thermal

analysis curve of PCNT-2 (Fig. S16, ESI†) exhibits two steps of weight loss: the first loss is from 40–300 °C, which corresponds to the loss of all water (free water and coordinated water), and the second loss is from 300–500 °C, arising from the decomposition of Trz organic molecules and carbon nanotubes.

The electrochemical performance of as-synthesized samples as anode materials for LIBs were investigated by assembling them into coin cells and cycling between 3.0 and 0.01 V vs. Li$^+$/Li. Fig. 3a and S17a† shows the comparative cycling performances of the PCNT-n, **Co-PMo**, **Co-PW**, pure CNTs, Trz ligand, (NBu$_4$)$_3$[PMo$_{12}$O$_{40}$] (abbreviated as NBu-PMo) and commercial graphite at a current density of 100 mA g^{-1}. The electrochemical performances of **Co-PMo** is better than that of **Co-PW**, which may be due to the excellent redox properties of Mo components in **Co-PMo**. It is obvious that the electrochemical performances of PCNT-n nanocomposites are better than that of bare **Co-PMo**, indicating an enhanced conductivity of PCNT-n nanocomposites due to the combination of CNTs, and among which PCNT-2 shows the highest capacities over the tested cycles. The first discharge capacity of PCNT-2 is as high as 1606 mA h g^{-1}, and the capacity loss in subsequent cycles could be ascribed to the formation of the SEI film, and the decomposition of the electrolyte.[38,39] After the first few cycles, the CE of PCNT-2 quickly improves to about 99%. After 100 cycles, the reversible capacities of PCNT-1 to 3 are stabilized at 670, 820 and 680 mA h g^{-1}, respectively, while the stable capacity of **Co-PMo** is 420 mA h g^{-1}. For comparison, **Co-PW**, NBu-PMo, Trz ligand, pure CNTs and commercial graphite achieve the capacity of 369, 121, 124, 415 and 323 mA h g^{-1} under the same testing conditions after 100 cycles, respectively. Besides, the electrochemical performance of physically mixed PCNT-2 (20 wt% CNTs, PM-

PCNT) is also tested and the reversible capacity is 585 mA h g^{-1}. All the above results indicate that PCNT-2 nanostructures as LIB anodes are superior to not only any single component but also the physically mixed PCNT-2, as well as doubling that of commercial graphite capacity, which can be concluded that the PCNT nanostructures can combine the advantages of POMs, MOFs and CNTs by the synergistic effects of the three.

The charge/discharge profiles of the PCNT-2 and **Co-PMo** anode for different cycle numbers are shown in Fig. 3b and S17b,† and the discharge process of the first few runs are different from the others due to the initial capacity loss. After that, the curves almost overlapped, indicating the formation of a stable solid electrolyte interphase (SEI) film and a good electrochemical reversibility of the electrode. Fig. 3c and S18† shows the cyclic voltammetry (CV) experiments at the range of 0.01–3.0 V (scan rate: 0.1 mV s^{-1}) for the first several cycles. For all materials, the irreversible reduction peaks around 0.6 V appear at the first cycle, then get smaller in the subsequent cycles due to the formation of SEI films. After the first round of stability, two broad peaks become apparent at the potential of 1.24 V for the reduction and 1.44 V for the oxidation in **Co-PMo** (1.20 V for the reduction and 1.36 V for the oxidation in **Co-PW**), which may be ascribed to the reduction and oxidation of the Mo (W) atoms.[34] By comparing PCN-2 with **Co-PMo**, it can be concluded that the combination of CNTs does not affect the redox peak. In addition, the smaller potential difference of 1.34 V (reduction) and 1.42 V (oxidation) in PCNT-2 proves that the polarization of the PCNT-2 electrode is smaller due to the good conductivity of PCNT-2. Moreover, PCNT-2 also works well in the rate performance at the current density of 100, 200, 500, and even to 1000 mA g^{-1}, giving the discharge specific capacity of $ca.$ 873, 811, 744, and 654 mA h g^{-1}, respectively. For comparison, **Co-PMo** achieves the specific capacity of $ca.$ 576, 408, 236 and 142 mA h g^{-1}, suggesting the enhanced performances after incorporation with CNTs. Note that the capacity can be restored to 820 mA h g^{-1} (Fig. 3d) when the current density resets to 100 mA g^{-1}, revealing the PCNT-2 electrode has a good reversibility. Further, at higher current densities of 2000 mA g^{-1} (Fig. 3e), the PCNT-2 electrode can also be stable with the capacity of 345 mA h g^{-1} for over 450 cycles without obvious capacity loss. To unravel the internal resistance of the battery, electrochemical impedance spectroscopy (EIS) was carried out to explore the electrochemical processes of the PCNT-2 composite. As shown in Fig. S19 (ESI†), the EIS of the untreated cell upon prolonged storage is presented. Apparently, the large semicircle grows along with increasing storage time until it gradually reaches a steady state, indicating the interface between the electrode and the electrolyte attains the metastable situation.[40] Compared with the pure **Co-PMo** cell (9 h), the PCNT-2 cell takes less time (5 h) to reach a stable state, indicating the electrolyte can rapidly be infiltrated into the PCNT composites, forming the initial SEI film. The charge-transfer resistances of the PCNT-2 electrode after the rest (~85 Ω) is approximately three times smaller than that of the **Co-PMo** electrode (~260 Ω), indicating that the conductivity is enhanced after incorporation with CNTs.
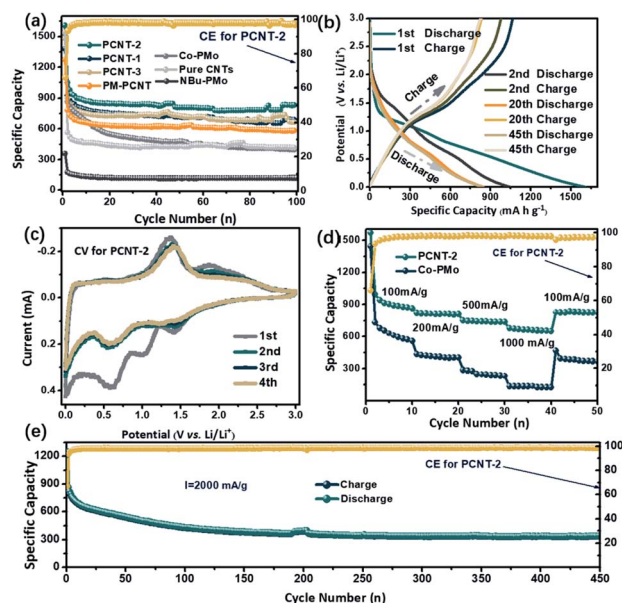

Fig. 3 Electrochemical performance of different electrodes. (a) Cycling performance at 100 mA g^{-1}. (b) Charge/discharge profiles for different cycles for PCNT-2. (c) Cyclic voltammetry of the PCNT-2 anodes at the range of 0.01–3 V (scan rate: 0.1 mV s^{-1}). (d) Cycling at various current densities (CE = coulombic efficiency). (e) Stability test of PCNT-2 for 450 cycles at 2000 mA g^{-1}.

This journal is © The Royal Society of Chemistry 2020

J. Mater. Chem. A, 2020, **8**, 25316–25322 | **25319**

To study the reaction mechanism of **Co-PMo**/CNTs nanocomposites for LIBs, the element compositions and valences of PCNT-2 were characterized in detail by *ex situ* X-ray photoelectron spectroscopy (XPS) of fresh and discharged/charged PCNT-2 (mixed with Super-P carbon and PVDF, at 1st-discharge to 0.01 V and 2nd-charge), respectively. The survey spectra are shown in Fig. 4a. In Fig. 4b, before the discharge of the PCNT-2 cell, the Mo 3d spectrum shows two main peaks at 232.5 and 235.8 eV that can be deconvoluted into four peaks at 234.2 eV, 231.1 eV, 235.1 eV and 232.1 eV, respectively, and are ascribed to Mo^{5+} $3d_{3/2}$ and Mo^{5+} $3d_{5/2}$, Mo^{6+} $3d_{3/2}$ and Mo^{6+} $3d_{5/2}$.[41] However, after discharging to 0.01 V, a part of the Mo species are reduced to Mo^{4+} because of the appearance of Mo^{4+} peaks at the binding energy of 231.9 eV.[42] Fortunately, when the PCNT-2 cell returned to 3 V, all the Mo species were transformed into Mo^{6+}, suggesting that the migration of Li-ions at the anode and cathode accompanies the transformation oxidation of Mo atoms. The C 1s spectra of both samples could be divided into three Gaussian peaks associated with C–C (284.6 eV), C–N (285.3 eV), and C=C (286.4 eV), respectively (Fig. 4c).[43] However, the new peaks at 290.3 (identified as C=O) and 289.4 eV (identified as C–O) appeared at 1st-discharge and 2nd-charge, probably due to the formation of the SEI film (the main composite is Li_2CO_3).[44] Before charging/discharging, the N 1s spectra shows three peaks, Co–N (400.3 eV),[45] pyridinic (399.7 eV) and pyrrolic N (398.5 eV) of the Trz ligand,[43] respectively. After Li-ion transfer to PCNT-2 material, the relative N content of Li–N (398.2 eV) appeared.[46] Note that the Li-ions anchored on the N atom at the initial discharge dissociated from the PCNT-2, indicating the good ability of the Trz ligand for Li^+ storage (Fig. 4d). In addition, SEM images demonstrate that the PCNT-2 electrode can still retain its natural morphology after discharge/charge reactions for 100 cycles (Fig. S20, ESI†).

The good reversible capacity and superior rate capability of PCNT-2 is much higher than the actual and theoretical capacity (calculated based on the XPS results, the valence change of metal ions and possible lithium ion storage sites of Trz ligands as detailed in ESI†) of **Co-PMo** and CNTs, which draws our attention to understand the kinetics origin. According to the theory of Dunn,[47–49] the actual capacity can be separated into three components: the faradaic contribution from the Li^+ insertion process, the charge-transfer process with surface atoms (referred to as pseudocapacitance) and non-faradaic electrical double layer capacitance (EDLC). The capacitive effects containing pseudocapacitance and EDLC can be characterized by analyzing CV data at various sweep rates. As shown in Fig. 5a and b, we tested the CV curves at different scan rates (0.2–1 mV s^{-1}) to confirm whether the Li storage is contributed by the capacitive behavior or not (fresh and after cycling cell) in the PCNT-2 cell. Generally, the relationship between the measured peak current (i) and sweep rate (v) in CV can be described by the power law $i = av^b$, where a and b both are constants, and the b-values can be determined from the slope of the plot of log(i) *vs.* log(v). It is well known that for diffusion-controlled processes, b approaches 0.5, while for surface capacitance-dominated processes, b is close to 1. As shown in Fig. 5c and d, the b value amounts to 0.819 for cathodic peaks and 0.911 for anodic ones in the fresh PCNT-2 cell, indicating the synergistic behavior of the capacitive effect and Li^+ insertion/extraction. After 50 cycles, the PCNT-2 cell exhibits relatively small b-values in both cathodic (0.596) and anodic (0.781) peaks, suggesting more favored insertion/extraction kinetics after cycling.

To evaluate the capacitive contribution to the total current response, we quantitatively separated the diffusion-controlled and surface capacitive contributions using the equation below:
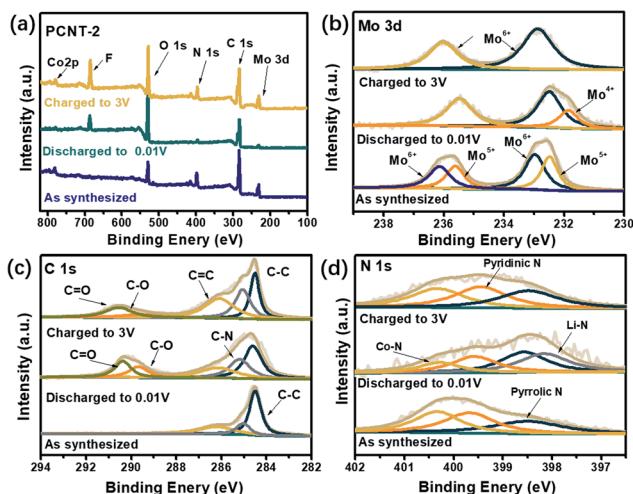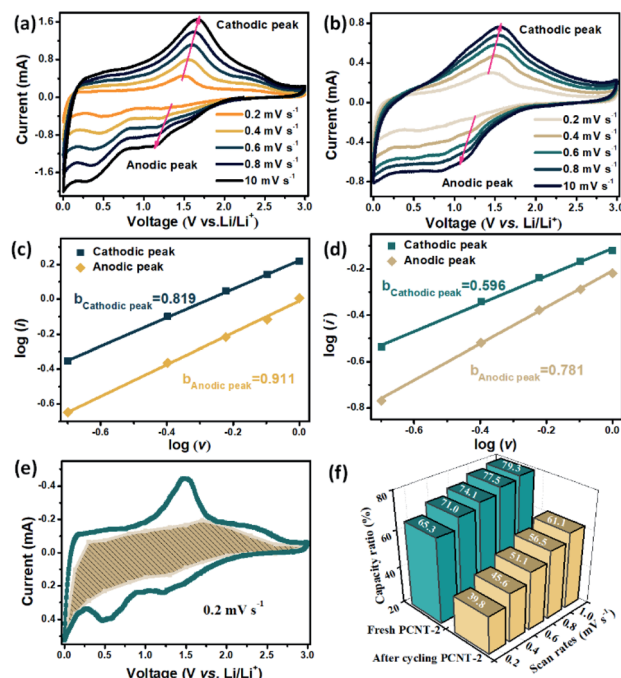

Fig. 5 CV curves at various scan rates from 0.2 to 1 mV s^{-1} of (a) fresh PCNT-2 cell and (b) after 50 cycles. The b-values determination by cathodic and anodic current peaks of (c) fresh PCNT-2 cell and (d) after 50 cycles. (e) Capacitive controlled charge storage contributions separated with cyclic voltammograms at 0.2 mV s^{-1} scan. (f) Capacitive-contribution ratio of fresh and after 50 cycles at different scan rates.

Fig. 4 XPS spectra of PCNT-2 before and after discharged at 0.01 V. (a) Survey scan, (b) Mo 3d, (c) C 1s, and (d) N 1s.

$$i(V) = k_1\nu + k_2\nu^{1/2}$$

where $i(V)$, $k_1\nu$, and $k_2\nu^{1/2}$ correspond to the total current response at a given potential, the current due to surface capacitive effects, and the current due to diffusion-controlled Li^+ insertion process, respectively. For analytical purposes, the above equation can be reformulated as:

$$i(V)/\nu^{1/2} = k_1\nu^{1/2} + k_2$$

By plotting $i(V)/\nu_{1/2}$ vs. $\nu_{1/2}$ at specific potentials between 0.01–3 V vs. Li^+, one can calculate the values of k_1 (slope) and k_2 (intercept) from the straight lines. This allows us to analyze the fraction of the current originating from surface capacitance and Li^+ diffusion at a specific voltage. The shaded area represents the voltage profile for the capacitive current response compared with the total measured current on a typical CV for the fresh PCNT-2 cell at a scan rate of 0.2 mV s^{-1} (Fig. 5e). The results show that the capacitive-controlled capacity accounts for ca. 65.3% of the total capacity. For comparison, we also calculated the capacitance-contribution of the PCNT-2 cell after 50 cycles, and the capacitive-controlled proportion is ca. 39.8%. This phenomenon can be explained by the relatively larger initial capacity caused by the unstable SEI film at the beginning several cycles, which may contain more capacitance-contribution capacity. As we all know, the higher the scan rate, the more the capacitive contribution. Obviously, in our case, the capacitive-controlled proportion at a scan rate of 1.0 mV s^{-1} increases to 79.3 and 61.1% for fresh and after cycling the PCNT-2 cell (Fig. 5f, S21 and S22, ESI†). The results indicate that the capacitive contribution plays a significant role in the total capacity, especially at higher current density, for the initial stage or after cycling.

Based on the discussion above, a possible mechanism for the cooperative capacity of the battery–supercapacitor behavior was proposed and is shown in Fig. 6. The battery behavior of the PCNT nanocomposite is achieved by coordination with Li^+ in the N-rich ligand moiety. Meanwhile, the capacitive-controlled contribution can be understood like this: the Mo atoms can take part in the redox reaction, forming the faradaic currents, which can compensate for part of the non-coordinated Li^+ ions (pseudocapacitance). There are additional Li^+ ions stored in the accessible interstitial sites on the interface or pores of PCNT-2 composites, with the charge being compensated by non-faradaic additional electrons on the CNTs surface (physical process, EDLC). Therefore, PCNT composites may offer a new and efficient platform for Li^+ ion storage with the hybrid behavior of battery and supercapacitor.

Conclusions

In conclusion, we have opened up a new route for preparing crystalline POMOFs by employing water–PEG 400 as reaction media. The two novel POMOFs exhibit a three-dimensional pillared Co-Trz framework with accessible channels. In addition, by consolidating the multi-electron redox properties of POMOFs with an open framework and the highly conductive carbon nanotubes, PCNT-n nanocomposites were successfully prepared and employed as an anode material toward LIBs. The resulting PCNT-2 can deliver a high capacity (820 mA h g^{-1} for 100 cycles) and excellent rate capability, and can bear a current density of 2000 mA g^{-1} over 450 cycles without obvious capacity loss. Nevertheless, the XPS results prove that the PCNT-2 nanocomposite could effectively expose the active anchored sites to bond Li^+ ions. The detailed electrochemical kinetic analysis of the PCNT-2 reveals its cooperative capacity of battery–supercapacitor behavior for superior energy storage. The successful synthesis of POMOF through a surfactant-assisted method and performance improvement nano-composites might guide the design of more POM-based micro/nano/single-crystal materials or their nanocomposites for extensive applications.

Conflicts of interest
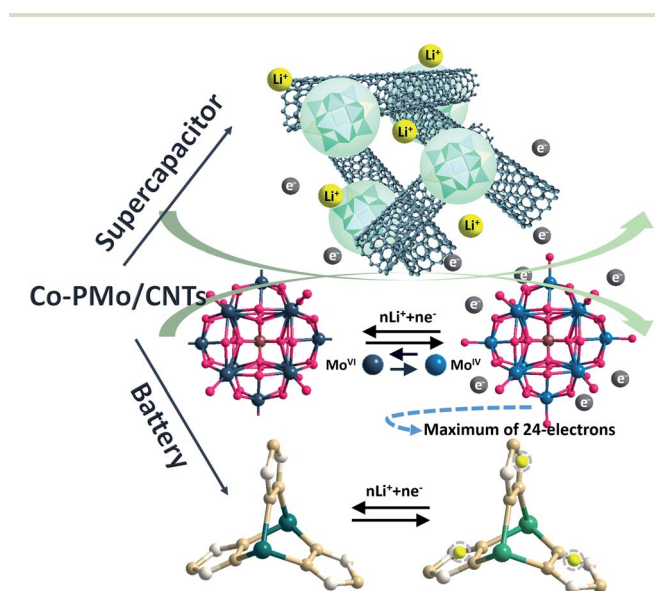
There are no conflicts to declare.

Acknowledgements

Fig. 6 The schematic diagram of the possible mechanism for the cooperative capacity of battery–supercapacitor for the PCNT nanocomposites.

Notes and references

1 M.-P. Santoni, G. S. Hanan and B. Hasenknopf, *Coord. Chem. Rev.*, 2014, **281**, 64–85.

This journal is © The Royal Society of Chemistry 2020

J. Mater. Chem. A, 2020, **8**, 25316–25322 | **25321**

2 V. Prabhakaran, B. L. Mehdi, J. J. Ditto, M. H. Engelhard, B. Wang, K. D. D. Gunaratne, D. C. Johnson, N. D. Browning, G. E. Johnson and J. Laskin, *Nat. Commun.*, 2016, **7**, 11399.

3 B. Huang, D.-H. Yang and B.-H. Han, *J. Mater. Chem. A*, 2020, **8**, 4593–4628.

4 L. Chen, W.-L. Chen, X.-L. Wang, Y.-G. Li, Z.-M. Su and E.-B. Wang, *Chem. Soc. Rev.*, 2019, **48**, 260–284.

5 D.-Y. Du, J.-S. Qin, S.-L. Li, Z.-M. Su and Y.-Q. Lan, *Chem. Soc. Rev.*, 2014, **43**, 4615–4632.

6 H. N. Miras, L. Vilà-Nadal and L. Cronin, *Chem. Soc. Rev.*, 2014, **43**, 5679–5699.

7 V. K. Abdelkader-Fernández, D. M. Fernandes, S. Balula, L. Cunha-Silva and C. Freire, *J. Mater. Chem. A*, 2020, **8**, 13509–13521.

8 J. Gao, M. He, Z. Y. Lee, W. Cao, W.-W. Xiong, Y. Li, R. Ganguly, T. Wu and Q. Zhang, *Dalton Trans.*, 2013, **42**, 11367–11370.

9 Y. Yin and A. P. Alivisatos, *Nature*, 2005, **437**, 664–670.

10 Y. Xia, P. Yang, Y. Sun, Y. Wu, B. Mayers, B. Gates, Y. Yin, F. Kim and H. Yan, *Adv. Mater.*, 2003, **15**, 353–389.

11 L. Peng, J. Zhang, J. Li, B. Han, Z. Xue and G. Yang, *Chem. Commun.*, 2012, **48**, 8688–8690.

12 L.-B. Sun, J.-R. Li, J. Park and H.-C. Zhou, *J. Am. Chem. Soc.*, 2012, **134**, 126–129.

13 J. Wei, Q. Yue, Z. Sun, Y. Deng and D. Zhao, *Angew. Chem., Int. Ed.*, 2012, **51**, 6149–6153.

14 H. Xu, F. Liu, Y. Cui, B. Chen and G. Qian, *Chem. Commun.*, 2011, **47**, 3153–3155.

15 W.-W. Xiong, E. U. Athresh, Y. T. Ng, J. Ding, T. Wu and Q. Zhang, *J. Am. Chem. Soc.*, 2013, **135**, 1256–1259.

16 W.-W. Xiong, P.-Z. Li, T.-H. Zhou, A. I. Y. Tok, R. Xu, Y. Zhao and Q. Zhang, *Inorg. Chem.*, 2013, **52**, 4148–4150.

17 Y. P. Wu, W. Zhou, J. Zhao, W. W. Dong, Y. Q. Lan, D. S. Li, C. Sun and X. Bu, *Angew. Chem.*, 2017, **129**, 13181–13185.

18 J. Zhao, Y. Wang, W. Dong, Y. Wu, D. Li, B. Liu and Q. Zhang, *Chem. Commun.*, 2015, **51**, 9479–9482.

19 J. Gao, Q. Tay, P. Z. Li, W. W. Xiong, Y. Zhao, Z. Chen and Q. Zhang, *Chem.–Asian J.*, 2014, **9**, 131–134.

20 J. Gao, K. Ye, L. Yang, W.-W. Xiong, L. Ye, Y. Wang and Q. Zhang, *Inorg. Chem.*, 2014, **53**, 691–693.

21 J. Gao, K. Ye, M. He, W.-W. Xiong, W. Cao, Z. Y. Lee, Y. Wang, T. Wu, F. Huo and X. Liu, *J. Solid State Chem.*, 2013, **206**, 27–31.

22 X. Yang, P. Zhu, J. Ren, Y. Chen, X. Li, J. Sha and J. Jiang, *Chem. Commun.*, 2019, **55**, 1201–1204.

23 G. J. Chen, L. Zhang, Y. D. Zhang, K. Liu, Z. Y. Long and Y. Wang, *J. Mater. Chem. A*, 2019, **7**, 7194–7201.

24 B. Iqbal, X. Y. Jia, H. B. Hu, L. He, W. Chen and Y.-F. Song, *Inorg. Chem. Front.*, 2020, **7**, 1420–1427.

25 S.-C. Huang, C.-C. Lin, C.-T. Hsu, C.-H. Guo, T.-Y. Chen, Y.-F. Liao and H.-Y. Chen, *J. Mater. Chem. A*, 2020, **8**, 21623–21633.

26 H. Wang, S. Hamanaka, Y. Nishimoto, S. Irle, T. Yokoyama, H. Yoshikawa and K. Awaga, *J. Am. Chem. Soc.*, 2012, **134**, 4918–4924.

27 Y. Nishimoto, D. Yokogawa, H. Yoshikawa, K. Awaga and S. Irle, *J. Am. Chem. Soc.*, 2014, **136**, 9042–9052.

28 X.-X. Li, F.-C. Shen, J. Liu, S.-L. Li, L.-Z. Dong, Q. Fu, Z.-M. Su and Y.-Q. Lan, *Chem. Commun.*, 2017, **53**, 10054–10057.

29 X.-Y. Yang, T. Wei, J.-S. Li, N. Sheng, P.-P. Zhu, J.-Q. Sha, T. Wang and Y.-Q. Lan, *Inorg. Chem.*, 2017, **56**, 8311–8318.

30 P.-P. Zhu, N. Sheng, M.-T. Li, J.-S. Li, G.-D. Liu, X.-Y. Yang, J.-Q. Sha, M.-L. Zhu and J. Jiang, *J. Mater. Chem. A*, 2017, **5**, 17920–17925.

31 Y.-Y. Wang, M. Zhang, S.-L. Li, S.-R. Zhang, W. Xie, J.-S. Qin, Z.-M. Su and Y.-Q. Lan, *Chem. Commun.*, 2017, **53**, 5204–5207.

32 Q. Huang, T. Wei, M. Zhang, L.-Z. Dong, A.-M. Zhang, S.-L. Li, W.-J. Liu, J. Liu and Y.-Q. Lan, *J. Mater. Chem. A*, 2017, **5**, 8477–8483.

33 W. Zhang, G. Jia, Z. Li, C. Yuan, Y. Bai and D. Fu, *Adv. Mater. Interfaces*, 2017, **4**, 1601241.

34 T. Wei, M. Zhang, P. Wu, Y.-J. Tang, S.-L. Li, F.-C. Shen, X.-L. Wang, X.-P. Zhou and Y.-Q. Lan, *Nano Energy*, 2017, **34**, 205–214.

35 X. Li, X.-Y. Yang, J.-Q. Sha, T. Han, C.-J. Du, Y.-J. Sun and Y.-Q. Lan, *ACS Appl. Mater. Interfaces*, 2019, **11**, 16896–16904.

36 J.-Q. Sha, X.-Y. Yang, Y. Chen, P.-P. Zhu, Y.-F. Song and J. Jiang, *ACS Appl. Mater. Interfaces*, 2018, **10**, 16660–16665.

37 C. Wang, M. Zhou, Y. Ma, H. Tan, Y. Wang and Y. Li, *Chem.–Asian J.*, 2018, **13**, 2054–2059.

38 J. B. Goodenough and K.-S. Park, *J. Am. Chem. Soc.*, 2013, **135**, 1167–1176.

39 L. Huang, J. Hu, Y. Ji, C. Streb and Y. F. Song, *Chem.–Eur. J.*, 2015, **21**, 18799–18804.

40 J. Song, H. Lee, Y. Wang and C. Wan, *J. Power Sources*, 2002, **111**, 255–267.

41 J. Xie, Y. Zhang, Y. Han and C. Li, *ACS Nano*, 2016, **10**, 5304–5313.

42 B. Dasgupta, Y. Ren, L. M. Wong, L. Kong, E. S. Tok, W. K. Chim and S. Y. Chiam, *J. Phys. Chem. C*, 2015, **119**, 10592–10601.

43 Y. Liu, N. Zhang, C. Yu, L. Jiao and J. Chen, *Nano Lett.*, 2016, **16**, 3321–3328.

44 A. C. Lim, H. S. Jadhav, H. J. Kwon and J. G. Seo, *ACS Omega*, 2019, **4**, 4129–4137.

45 K. Burger, C. Várhelyi, E. Fluck, H. Binder and I. Speyer, *Z. Anorg. Allg. Chem.*, 1974, **408**, 304–312.

46 M. Kaplunov, Y. M. Shuwa, K. Pokhodnya and Y. G. Borodko, *Phys. Status Solidi B*, 1976, **73**, 335–339.

47 P. Simon, Y. Gogotsi and B. Dunn, *Science*, 2014, **343**, 1210–1211.

48 J. Wang, J. Polleux, J. Lim and B. Dunn, *J. Phys. Chem. C*, 2007, **111**, 14925–14931.

49 V. Augustyn, P. Simon and B. Dunn, *Energy Environ. Sci.*, 2014, **7**, 1597–1614.

25322 | *J. Mater. Chem. A*, 2020, **8**, 25316–25322

This journal is © The Royal Society of Chemistry 2020